Digital synthesis of free-form multimaterial structures for realization of arbitrary programmed mechanical responses

Weichen Li[a], **Fengwen Wang**[b], **Ole Sigmund**[b], **and Xiaojia Shelly Zhang**[a,c,1]

[a]Department of Civil and Environmental Engineering, University of Illinois Urbana-Champaign, 205 North Mathews Ave, Urbana, IL 61801, USA; [b]Department of Mechanical Engineering, Technical University of Denmark, Nils Koppels Alle, Building 404, 2800 Kongens Lyngby, Denmark; [c]Department of Mechanical Science and Engineering, University of Illinois Urbana-Champaign, 1206 W. Green St., Urbana, IL 61801, USA

Programming structures to realize any prescribed mechanical response under large deformation is highly desired for various functionalities, such as actuation and energy trapping. Yet, the use of a single material phase and heuristically developed structural patterns leads to restricted design space and potential failure to achieve specific target behaviors. Here, through a free-form inverse design approach, multiple hyperelastic materials with distinct properties are optimally synthesized into composite structures to precisely achieve arbitrary and extreme prescribed responses under large deformations. The digitally synthesized structures exhibit organic shapes and motions with irregular distributions of material phases. Within the structures, different materials play distinct roles yet seamlessly collaborate through sophisticated deformation mechanisms to produce the target behaviors, some of which are unachievable by a single material. While complex in geometry and material heterogeneity, the discovered structures are effectively manufactured via multimaterial fabrication with different Polydimethylsiloxane (PDMS) elastomers with distinct behaviors, and their highly nonlinear responses are physically and accurately realized in experiments. To enhance programmability, the synthesized structures are hetero-assembled into architectures that exhibit highly complex yet navigable responses. The proposed synthesis, multimaterial fabrication, and hetero-assembly strategy can be utilized to design function-oriented and situation-specific mechanical devices for a wide range of applications.

Complex mechanical response | Multimaterial fabrication | Digital synthesis | Large deformation | Topology optimization

Programming structures to realize arbitrary mechanical response is invaluable for applications such as soft robotics (1–3), energy absorbers (4–8), and flexible electronics (9–12). Advanced functionalities are achieved based on various mechanical responses (force-displacement or stress-strain relations) with distinct function-oriented features. Considerable advances in response programming have been made through varying structural geometry (i.e., feature sizes, cellular patterns, hole shapes, structural topology, deformation states) (2, 4, 6, 8, 10, 11, 13–22), assembly sequence (5, 7, 23–25), and external confinement (26), which produce responses including stiffening, softening, multistable, buckling, and auxetic behaviors. Most of the established metamaterials are based on heuristically developed patterns or usage of a single constituent material. However, some highly complex yet desirable responses cannot be precisely attained solely through the adjustment of heuristic patterns or using a single material (27), as they could leave out a plethora of uncharted patterns that can potentially outperform traditional designs (28). In contrast to engineered designs, structures in nature exhibit complex and irregular geometry and are comprised of multiple materials with dissimilar properties optimally collaborating to produce different biological functions (29). Hence, an optimization-guided free-form synthesis procedure with multiple distinct materials can significantly enlarge the design space exploration, which in turn yields a powerful strategy to program metastructures' response. However, such advantage has not yet been exploited partly due to a lack of intelligent synthesis approach capable of integrating different materials with free-form geometry to accomplish advanced nonlinear functionality.

Through an algorithmic procedure, this study harnesses multiple nonlinear materials and free-form geometry to optimally synthesize composite metastructures that precisely achieve arbitrary and complex prescribed responses. This algorithm-based design process is hereby referred to as "digital synthesis". The synthesis encodes the intelligence of material phase selection, distribution, and geometric variation through a computational morphogenesis technique known as topology optimization (30). Within a spatial domain, topology optimization adds, removes, or alters material to minimize a user-defined objective function. In this study, the objective

Significance Statement

Creating structures to realize function-oriented mechanical responses is desired for many applications. Yet, the use of a single material phase and heuristics-based designs may fail to attain specific target behaviors. Here, through a deterministic algorithmic procedure, multiple materials with dissimilar properties are intelligently synthesized into composite structures to achieve arbitrary prescribed responses. Created structures possess unconventional geometry and seamless integration of multiple materials. Despite geometric complexity and varied material phases, these structures are fabricated by multimaterial manufacturing, and tested to demonstrate wide-ranging nonlinear responses are physically and accurately realized. Upon hetero-assembly, resulting structures provide architectures that exhibit highly complex yet navigable responses. The proposed strategy can benefit the design of function-oriented nonlinear mechanical devices, such as actuators and energy absorbers.

Author contributions: XSZ, OS, FW designed research; WL, XSZ performed research; WL, FW, OS, XSZ analyzed data; WL, XSZ wrote the paper; and WL, FW, OS, XSZ edited the paper.

The authors declare no competing interests.

[1]To whom correspondence should be addressed. E-mail: zhangxs@illinois.edu

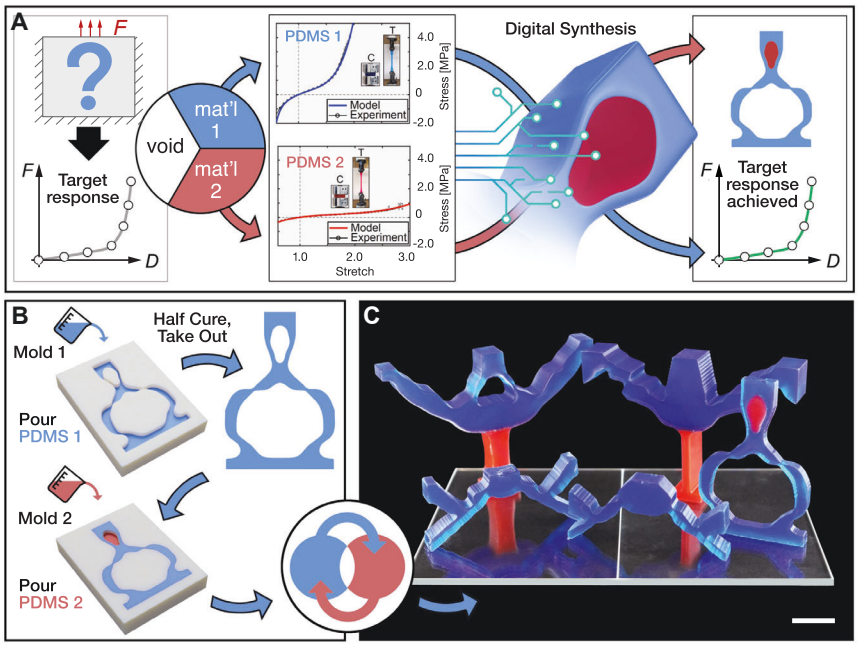

Fig. 1. Digital synthesis and hybrid fabrication of multimaterial structures using two PDMS elastomers with distinct properties that seamlessly collaborate to achieve prescribed target response. (A) Illustration of the multimaterial digital synthesis procedure to achieve target response. The stress-stretch curves of the two materials are fitted based on uniaxial test data. (B) The proposed two-level molding and casting hybrid fabrication process. (C) Selected fabricated multimaterial specimens. (Scale bars: 20 mm.)

function is the error between actual and prescribed target responses. (For more details about the algorithmic procedure, refer to Supporting Information Note S1.) The synthesized metastructures exhibit organic geometries and motions with irregular distribution of different material phases. Within the structure, different materials play distinct roles yet seamlessly collaborate through sophisticated deformation mechanisms (e.g., mechanical instability, large rotation, material heterogeneity, and material nonlinearity) to attain various families of unique target responses, including swift stiffening, large-deformation buckling, multistability, and long force plateaus.

Fabrication of the digitally synthesized structures is challenging owing to the complex geometry, multiple material phases, and large deformation requirement; the latter often requires the use of elastomers, which have been widely adopted to fabricate metamaterials (13, 14, 16, 26, 31). Most studies use a single material or relatively structured patterns while others require state-of-the-art 3D/4D printing technologies. Here, we use two PDMS elastomers with vastly different behaviors and a proposed inexpensive manufacturing method to accurately fabricate the digitally synthesized multimaterial structures. The fabricated specimens are tested, and their behaviors exhibit high agreement with the target responses. Various families of extreme and highly nonlinear behaviors are physically and precisely realized by the fabricated digitally-synthesized multimaterial structures with optimal geometry.

To extend the dimension of programmability, the created structures are used as building blocks and assembled into heterogeneous material architectures that exhibit highly complex yet navigable responses. Different from many assembled metamaterials, which use the same or similar building blocks (5, 7, 24, 25, 32), the constructed architecture herein are composed of diverse synthesized structures with distinct geometries and behaviors. Such hetero-assembly effectively enlarges the design space and enables the realization of many extreme responses that would otherwise be unattainable.

Results and Discussions

The digital synthesis procedure is illustrated in Fig. 1A. Given a design domain in space, a user-prescribed force-displacement relation, and two different materials, topology optimization concurrently optimizes the shape, material phase, and material distribution to form composite structures that accurately achieve the target. (Refer to Supporting Information Note S1 for more details). The digitally synthesized multimaterial structures are fabricated using two different PDMS elastomers (10:1 and 20:1 agent-base ratios, hereafter denoted as PDMS 1 and PDMS 2, respectively. See Supporting Information Note S2 for fabrication details of the specimens.) through a proposed multimaterial two-level molding and casting process shown in Fig. 1B (See Supporting Information Note S3 & S4 for details). Selected fabricated specimens are shown in Fig. 1C. As shown in the stress-stretch plots of Fig. 1A, the behaviors of the two PDMS are vastly different in stress magnitudes, nonlinear stiffness, maximum deformation, and the overall shape of the stress-stretch curve. As revealed in later sections, this big difference is vital to the precise realization of certain responses in which the two materials play distinct roles yet collaborate seamlessly through sophisticated deformation mechanisms.

Swift stiffening produced by frog-like geometry. We first study a family of swift-stiffening responses shown in Fig. 2B. Through the digital synthesis, we obtain the irregular yet visually organic, frog-like structure (Dsg. I) as shown in Fig. 2A. The undeformed configuration is similar to a sitting frog with two curved legs. When loaded upward, the deformed configuration resembles a jumping frog with two straight legs. As shown in Fig. 2B, the frog-like shape and deformation produce a response that accurately achieves the prescribed stiffening behavior in both experiment and simulation. (See Supporting Information Movie S1 for the digital synthesis and experimental validation of the frog-like structures.)

The creation of the frog-like geometry and resulting "jump-

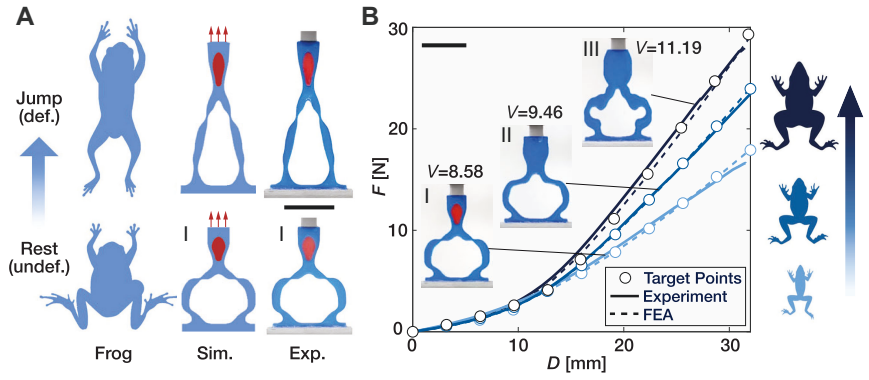

Fig. 2. Synthesized structures with frog shapes programmed with swift stiffening responses. (A) A multimaterial frog-like structure: deformed and undeformed configurations, resembling resting and jumping states of a frog. (b) Synthesized frog-like structures programmed with various target stiffness and comparison of target, experimental, and simulation responses. (Scale bars: 40 mm.)

ing" deformation is intimately related to the prescribed requirement of rapid stiffening. During the first phase of loading (the low-stiffness phase of the target response), the two "legs" attached to the bottom are curved; hence, they deform in a flexure-dominated mode that yields low stiffness. In the second phase featuring the high stiffness, the curved "legs" straighten and switch from the flexure-dominated mode to a stretch-dominated mode; this yields the acute increase in stiffness. We remark that the small red region (made of PDMS 2) has a strong impact on the actual response and fitting accuracy of Dsg. I. (See Supporting Information Note S5 A for detailed analysis.)

Increase in the stiffness of the second-phase target response effectively boosts the structural volume and member sizes. This is demonstrated in the three structures (Dsgs. I - III) in Fig. 2B, where stiffer target responses lead to higher total volume, thicker "legs", and larger "bodies", developing more powerful "jumps". As shown in Fig. 2B, the three experimental responses precisely match the corresponding targets. Notably, unlike the first structure, the two stiffer structures are assigned with PDMS 1 only. This is because PDMS 1 is more efficient in realizing stiffer responses than the softer PDMS 2.

Diverse buckling responses through isovolumetric shape variation. Next, we aim to create a family of buckling-dominated structures with force-displacement relations precisely programmed over the entire loading history. The target responses are characterized by five linear-sinusoidal curves (Fig. 3A) with diverse overall stiffness and force magnitudes. The curves are defined by $F(D) = \alpha D + \beta \sin(\frac{2\pi}{D_{max}} D)$ with varied coefficients α and β. Note that the two bottom curves pass through the zero-force axis, indicating multistability. While nonlinear elastic buckling has been extensively studied, how to accurately achieve prescribed behaviors (e.g., force, stiffness, and dissipated/stored energy) over the complete loading history remains challenging. Such high-precision control of buckling is highly desired in applications such as recoverable energy dissipation (7), energy trapping (8), and actuation (2).

The digital synthesis yields the five optimized structures (Dsgs. IV - VIII) in Fig. 3A along with their experimental and simulated responses. All designs feature a relatively bulky "body" in the center with one arm connected to each side. Each side-arm then branches into two members, which are attached to the support. These geometric features induce buckling of the two arms and large rotation concentrated at the thin joints of the arms, which in turn produce the sinusoidal behaviors. Based on whether the force-displacement curves pass through the zero-force axis, the five structures can be categorized into two distinct mechanical behaviors, i.e., self-recoverable and self-locking; the latter remains at their second stable configuration (Fig.3A) when force is removed.

For Dsgs. V - VIII (excluding Dsg. IV), the two end arm branches grow toward the center, and the middle bulk member, as well as the joints, decrease in size. These geometric variations cause a gradual decrease in the overall stiffness and force. While irregular in geometry, all structures are synthesized with PDMS 1 only, although both PDMS are considered as candidate materials in the design process. The preference of PDMS 1 over PDMS 2 in this set of results is related to the high stiffness and force variation required by the particular target responses. Given the small material usage constraint (15% of the domain volume) and the dominant role of kinematics and buckling, the stiffer PDMS 1 is more efficient than PDMS 2 in realizing the large stiffness and force variations in this series of target shapes Interestingly, although the stiffness and force of the five structures are drastically different, the volume and overall topology are identical. This demonstrates that solely varying the perimeter of the structure is sufficient to precisely achieve the diverse responses. This unique feature is not seen in traditional beam-like buckling structures where larger overall stiffness is realized through thicker members and larger volumes. As shown in Fig. 3A, despite minor deviations in the initial stage, the experimental responses accurately achieve the targets and exhibit good agreement with the simulated responses. (See Supporting Information Movies S2 for comparison of the experimental and simulated results for Dsg. VIII.)

The self-recoverable elastic buckling and self-locking multistability can be used to dissipate and store energy. The amount of dissipated energy is the area of the force-displacement loop illustrated in the top left plot of Fig. 3B, and the amount of stored energy at the second stable configuration is equal to the subtraction of negative work from positive work as shown in the bottom left plot of Fig. 3B. The (experimental) energy profile of these five structures is shown on the right plot of Fig. 3B. For dissipation, structures with lower overall stiffness consume more energy as a result of the larger loop area; for storage, the structure with higher stiffness (Dsg. VII) traps more energy due to the smaller negative work. As energy (dissipated and stored) is a derivation of force-displacement responses, it is also accurately programmable using the proposed digital synthesis.

The distinct mechanical behaviors between self-recovering and self-locking are caused by small yet critical geometric vari-

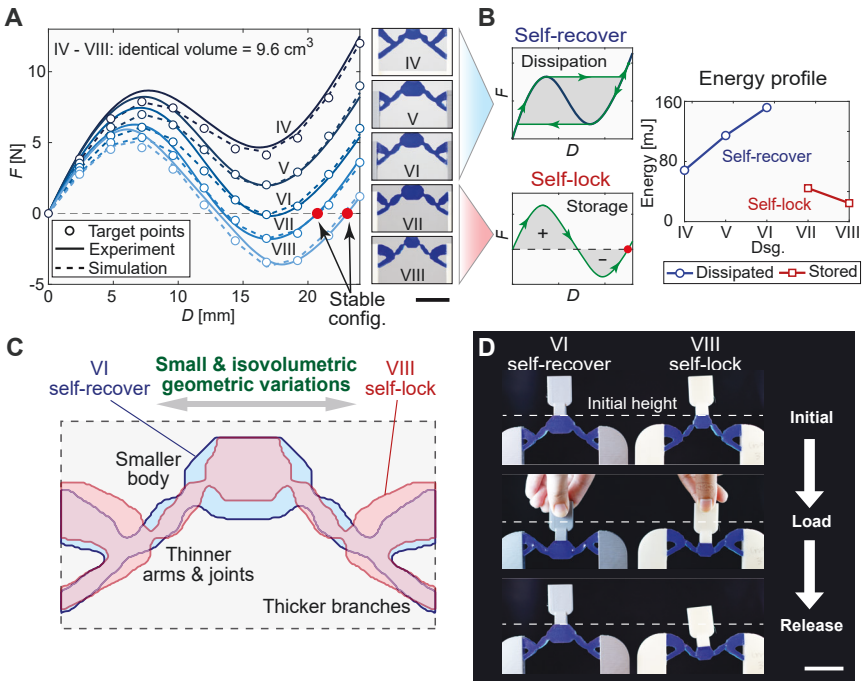

Fig. 3. Family of buckling-dominated structures synthesized with five different linear-sinusoidal target responses. (A) Five synthesized structures (specimens) with identical volumes and corresponding target, experimental, and simulation responses. The five designs are categorized into two distinct mechanical behaviors: self-recoverable and self-locking. (B) Illustration of dissipated and stored energy in self-recoverable and self-locking structures. Top left: self-recoverable energy dissipation due to force snap-through and snap-back; bottom left: self-lock energy storage at the second stable configuration; right: experimental dissipated energy of Dsgs. IV - VI and experimental stored energy of Dsgs. VII and VIII. (C) Comparison of geometries of Dsgs. VI (self-recoverable) and VIII (self-locking) shows subtle geometric difference. (D) Experiments demonstrate the distinct behaviors of the synthesized self-recoverable Dsg. VI and self-locking Dsg. VIII, respectively. (Scale bars: 40 mm.)

ations. As shown in Fig. 3C, the shapes of Dsgs. VI and VIII differ slightly in the size of the center body, arms, joints, and arm branches, yet, this subtle geometric difference severely alters the mechanical responses (from self-recovering to self-locking). This is further demonstrated in the experiment in Fig. 3D, where the two structures are both manually loaded to a deformed state then released. When released, Dsg. VI snaps back and (elastically) recovers its initial configuration as indicated by the white dashed line. By contrast, Dsg. VIII locks itself at the second stable configuration. (See Supporting Information Movie S3 for the complete recording of this experiment.)

Tunable long plateau behaviors by elastic stiffness phase transition. We now focus on realizing long force plateau behaviors under large deformation (Fig. 4A displays the corresponding collection of four synthesized structures), which is desired in applications such as vibration isolation. Specifically, we aim to achieve tunable long plateau behavior. As shown in Fig. 4B, it consists of a stiff and linear initial phase followed by the horizontal plateau phase spanning a displacement range (20 mm) twice to that of the first phase (10 mm). The long plateau is similar to the "yielding" behavior in ductile metals. Realizing the long plateau with purely elastic materials are highly challenging as the underlying mechanism can be complex. While certain developed metamaterials can exhibit plateau behaviors (13, 14), how to systematically and accurately tune their response such as plateau force magnitude ("yield" strength) and turning-point displacement ("yield" strain) under large deformation remains unsolved.

The corresponding synthesized multimaterial structure (specimen) at various loading stages is shown in Fig. 4B, along with the structure's target and programmed responses (experiment and simulation). The multimaterial structure features an upper part made of PDMS 1 with two arms attached to the side supports and a lower slender bar made of PDMS 2 connecting to the bottom. When loaded upward, the two side arms are compressed, and the bottom member is stretched, collectively yielding the initial linear and stiff response. As shown in Fig. 4B Stages a. and b., the structure before yielding has straight and compressed arms with the axial compression force transmitting from the side supports through a straight load path. At this stage, both the arms and bar provide positive stiffness as indicated by the "++" signs in Fig. 4B Stage b. When 10.0 mm displacement is approached, the two compressed arms buckled, causing an abrupt decrease in stiffness and entry of the plateau phase as indicated in Stage c. of Fig. 4B. The buckled and rotated arms trigger a stiffness phase transition from positive-positive (++) to positive-negative (+-). The almost-zero stiffness of the plateau originates from the combined effect of the positive stiffness from the uniaxially stretching bottom member and the negative stiffness from the buckled arms, as indicated in Stage c. of Fig. 4 B. Note that these two types of stiffness have different natures; the positive stiffness of the uniaxially stretching PDMS 2 member is from the nonlinear material property, whereas the negative stiffness from the buckling and rotation is governed by kinematics and geometry. (See Supporting Information Movie S4 for the entire deformation process and a comparison of the simulation and experimental results for Dsg. IX). Thus, the two PDMS materials play distinct roles, and the optimal integration of the two mechanisms leads to the stiffness phase change and yields the zero-stiffness plateau. When loaded further, the positive-negative stiffness phase remains (Stage d. of Fig. 4 B) and yields the complete long plateau. As shown in Fig. 4B, despite the complex mechanism and irregular geometry, the prescribed plateau response is accurately realized in the experiment.

By optimally varying the structural geometry, material distribution, and member sizes, the plateau force magnitude ("yield" strength) as well as the turning-point displacement ("yield" deformation) can be effectively programmed, a key difference from heuristically developed structures. This is

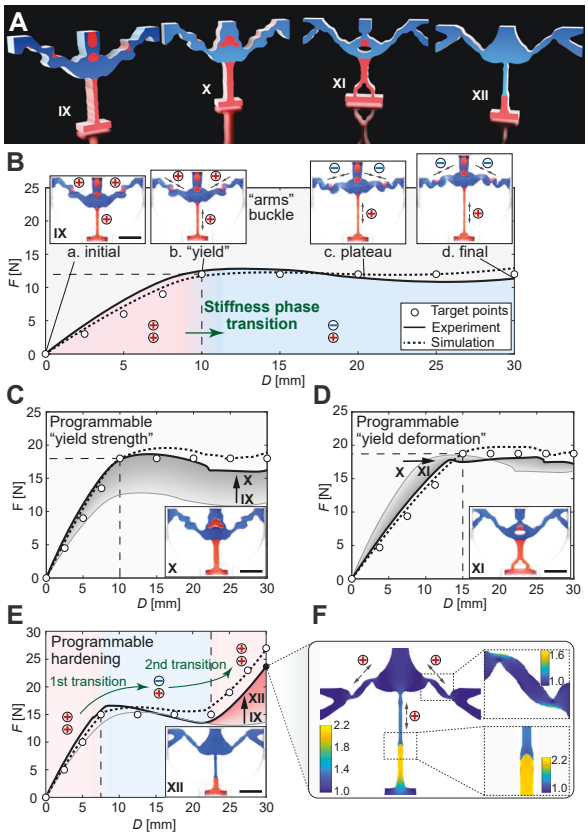

Fig. 4. Synthesized multimaterial structures programmed with diverse force plateau responses. (A) Collection of 3D synthesized structures (models) with different plateau behaviors. (B) Target, experimental, and simulated responses of Dsg. IX. The turning-point displacement is 10 mm. The "+" and "-" indicate positive and negative stiffness, respectively; inset: configurations (experiment) of Dsg. IX at four stages. (C & D) Synthesized structures and corresponding experimental and simulated responses programmed with a higher "yield" strength and a larger "yield" deformation, respectively; insets: undeformed configurations (experiment) of Dsgs. X and XI, respectively. (E) Synthesized structures and corresponding experimental and simulated responses programmed with a trilinear response with a final hardening phase; inset: undeformed configuration (experiment) of Dsg. XII. (F) Fringe plot of maximum principal stretch of Dsg. XII at the final deformed configuration. (Scale bars: 30 mm.)

demonstrated in the two synthesized structures in Fig. 4C and D, which are programmed with a higher plateau force and a larger turning point displacement, respectively. Compared to Dsg. IX, Dsg. X forms thicker arms and bottom bar but with a similar overall geometry. While effectively boosting the plateau force, these changes do not perturb the length of plateau, turning point displacement, and underlying stiffness phase transition. By contrast, to realize a larger "yield" deformation from Dsg. X, Dsg. XI fundamentally alters the topology and geometry as shown in Fig. 4D. Openings are generated in the middle of the structure and at the bottom, and branches appear near the end of the arms. Also, the size of the connection to the loading area significantly decreases compared to Dsg. X. While retaining the high plateau force, these features effectively reduce the stiffness for the linear phase, producing a larger "yield" deformation. We note that the tunable "yield" strength and deformation can also be realized in bilinear responses with even longer plateaus. See Supporting Information Note S6 for extended investigations.

Despite the different responses, Dsgs. IX - XI have small PDMS 2 (and void, for Dsg. XI) regions with irregular shapes at the upper half of the structure surrounded by PDMS 1. These regions, although relatively small and soft, have a non-negligible impact on the actual force-displacement response. The removal or modification of these regions, in general, would deteriorate the fitting accuracy of the structural response (See Supporting Information Note S5 B for detailed investigations). The importance of these multimaterial geometric details also demonstrates the high programming accuracy of the digital synthesis approach.

Beyond bilinear responses, a more complex trilinear response with a final hardening phase after the plateau can also be accurately realized under the same loaded displacement. This is demonstrated by the synthesized Dsg. XII in Fig. 4 E. The trilinear response is facilitated by two stiffness phase transitions, from "++" to "+-", then back to "++", as indicated in Fig. 4 E. The dual transition is produced by several critical geometric features different from those in Dsgs. IV-VI, where only a single transition takes place. First, the two arms (excluding the branches) are connected to the body at a higher location than Dsgs. IV-VI. Hence, at the final loading stage, the arms rotate to a reversed direction and undergo axial stretch, providing positive stiffness and enabling the second stiffness phase transition, i.e., from "+-" to "++". The large rotation is demonstrated in the final deformed configuration in Fig. 4 F, where the two arms rotate to a reversed 45 degree with respect to the horizontal axis. By contrast, the two arms in Dsgs. IV-VI only rotate to the horizontal direction (e.g., Stage d. of Fig. 4 B) and remain in compression. Second, the bottom PDMS 2 bar is significantly shorter than the other structures, and therefore, the stretch and stress are much higher under the same loaded displacement, which also boosts the stiffness at the final hardening stage. The large axial deformation is shown in the fringe plot of maximum principal stretch (simulation) in Fig. 4 F where the stretch reaches 2.2. Fig. 4 F also shows the large disparity of deformation magnitudes between the two materials. Despite the high stiffness at the initial and final stages, the plateau behavior in the middle phase is unperturbed. As shown in Fig. 4 E, the experimental and simulated force-displacement curves accurately match the prescribed response. We would like to emphasize that the trilinear response could not be precisely achieved had only

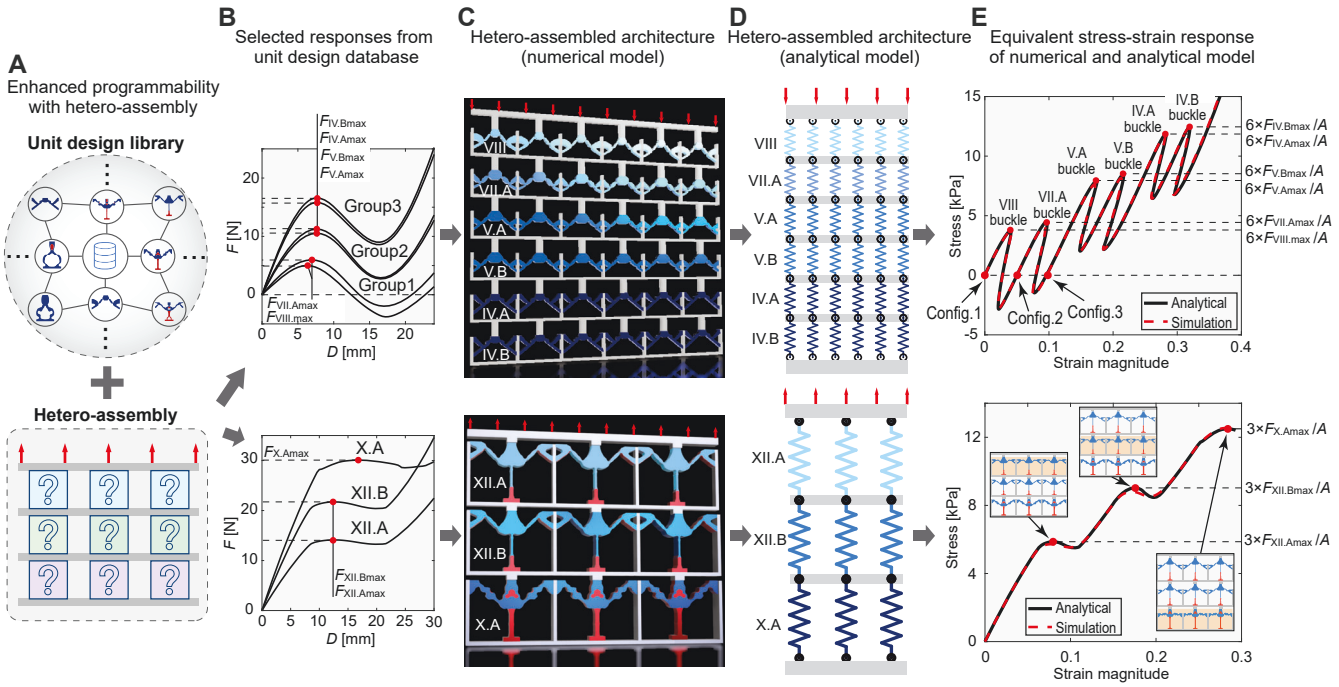

Fig. 5. Hetero-assembly of programmed structures into heterogeneous architectures with highly complex but navigable responses. (A) Illustration of library of unit structures (programmed structures) and hetero-assembly. (B) Two families of responses from selected programmed structures. Top: the first family features various buckling responses; bottom: the second features (bilinear and trilinear) long plateau responses. (C) Hetero-assembled architectures using corresponding unit structures in (B). Top: assembled architecture of multibuckling response; bottom: assembled architecture of multiplateau response. (D) Analytical reduced-order nonlinear spring models of top: multibuckling architecture; bottom: multiplateau architecture. (E) Highly complex yet programmable responses produced by the hetero-assembled architectures. Top: multibuckling response with three stable configurations and six buckling stages; bottom: multiplateau response with three force stairs.

one material been used. The additional investigation into one-material structures is provided in Supporting Information Note S7.

Multibuckling and multiplateau behaviors by hetero-assembled architecture. The various families of validated programmed structures constitute a library of diverse nonlinear behaviors and can be used as building blocks to construct heterogeneous architectures (Fig. 5 A) that exhibit highly complex but navigable responses for many advanced applications. To precisely control and efficiently guide the assembly process, we develop an analytical reduced-order nonlinear spring model (See Supporting Information Note S8). Each spring represents a programmed structure (building block) with two degrees of freedom (DOFs), i.e., the displacements at the two ends. The spring is characterized by a force-displacement response identical to the corresponding programmed structure. Based on the reduced-order model, the assembled architecture is converted to a network of nonlinear springs with a drastically reduced analytical cost.

By harnessing the differential peak forces in the various buckling-dominated structures (top plot of Fig. 5 B), we assemble an architecture that exhibits a hierarchical multibuckling and multistable response with controllable peak forces. As shown in the first plot of Fig. 5 C, the architecture is assembled by 6 × 6 programmed structures of Dsgs. IV, V, and VII with different thicknesses (labeled A and B), and Dsg. VIII. The Dsg. -IV.B, -IV.A, -V.B, -V.A, -VII.A, and -VIII thicknesses are 20.0, 19.0, 15.0, 14.0, 11.0, and 10.0 mm, respectively. The thickness variation is harnessed to tune the building block's force magnitudes so that those responses can be classified into three groups (Groups 1, 2, and 3 in Fig. 5 B) with three distinct overall force levels. Two unit designs in the same group have mildly differentiated force magnitudes. Note that both Dsgs. VII and VIII have two stable configurations. The corresponding reduced-order spring system is shown in the first plot of Fig. 5 D and produce a multistable and multibuckling response with six peaks (the first figure of Fig. 5 E, the force and displacement are normalized with respect to the cross-sectional area and initial height of the architecture, respectively, to obtain the equivalent axial stress and strain). The complex behavior arises from the programmable buckling sequence involving the six unit designs with differentiated peak forces. When loaded, Dsgs. VIII and VII.A buckle first because of their low peak forces ($F_{\mathrm{VIII.max}}$ and $F_{\mathrm{VII.Amax}}$), yielding the two multistable configurations (Configs. 2 and 3 in the first plot of Fig. 5 E). With continued loading, the force steadily increases until the peak forces of Dsgs. V.A and V.B ($F_{\mathrm{V.Amax}}$ and $F_{\mathrm{V.Bmax}}$) are reached; hence, consecutive buckling of those units occurs. When loaded further, the force increases stably again before the highest peak forces ($F_{\mathrm{IV.Amax}}$ and $F_{\mathrm{IV.Bmax}}$) are reached; this induces consecutive buckling of Dsgs. IV.A and IV.B. The sequential buckling of this heterogeneous architecture also exhibits a multilevel behavior in that the six sawtooth responses constitute three stairs (corresponding to the three groups) with different overall force levels. This type of multibuckling response is desirable in recoverable energy absorbers for impacts with wide-ranging intensity. The multistability can be harnessed to realize morphing and deployable structures (33–36).

Assembling the programmed structures with bilinear (Dsg. X) and trilinear (Dsg. XII) responses (bottom plot of Fig. 5 B)

leads to multiplateau responses with designable long plateau forces. As shown in the second plot of Fig. 5 C and D, the architecture is composed of the bilinear Dsg. X.A and trilinear Dsgs. XII.B and XII.A, with thickness of 24.0, 20.0, and 13.0 mm, respectively, and exhibits an extreme three-plateau response. This unique behavior is also due to the sequential hetero-assembly of the three unit designs with differentiated plateau forces and the third phase of the trilinear responses (i.e., hardening). When loaded under tension, all unit designs first exhibit their respective linear responses, which yields an initial linear metastructure behavior. As loading continues, the trilinear Dsg. XII.A reaches its plateau phase first because it has the lowest peak force among the three designs. At that stage, the total output force of the architecture remains almost constant even though the displacement continues to increase. The displacement is solely due to the continuing deformation of Dsg. XII.A, whereas the deformations of the other two units temporarily remain static. As loading progresses, the trilinear Dsg. XII.A reaches its final stiffening phase, and the total force of the architecture (along with the forces of the other two designs) begins to increase again; this yields the middle linear stiff phase of the multiplateau response. Under the same mechanism, continued loading yields the sequential realizations of the second and third plateaus, which are controlled by the peak forces of Dsgs. XII.B and X.A, respectively. As a result, all three plateau forces are accurately tuned by adjusting the plateau force magnitudes of the three unit designs. Fig. 5 E shows consistent computed responses by both full finite element analysis (FEA) and analytical reduced-order models. This multiplateau response is desirable for quantifiable, multilevel force control for vibration isolation devices (25) (see Supporting Information Movie S5 for the entire deformation process and a comparison between the analytical model and FEA for the third multimaterial architecture).

Concluding remarks. Multiple hyperelastic materials with distinct behaviors are optimally synthesized through an algorithmic procedure to physically and precisely realize a wide range of prescribed nonlinear mechanical responses. The synthesized multimaterial structures possess unconventional and organic geometry with biological features and irregular material distributions. Two materials in the synthesized structures seamlessly collaborate to comprehensively and intelligently exploit disparity of nonlinear material behaviors, change of deformation mode, buckling, large rotation, and stiffness phase transition to accurately deliver the desired response. Further, the programmed structures are fabricated through multimaterial manufacturing and can be assembled into heterogeneous architectures that exhibit highly complex but navigable behaviors. The proposed digital synthesis approach, validated composite structures, multimaterial fabrication, and hetero-assembly expand the scope of what is achievable for programmable mechanical metastructures/metamaterials.

Materials and Methods

Details of the multimaterial topology optimization are provided in Supporting Information Note S1. Fabrication, characterization, test, and modeling of PDMS elastomers and fabrication of synthesized structures are described in Supporting Information Note S2-S4. Influence of small regions with PDMS 2 on the response of Dsg. I and Dsg. IX - X are provided in Supporting Information S5. Extended investigations about bilinear responses with long plateaus and trlinear responses programmed with single material are provided in Supporting Information Note S6 and S7, respectively. Technical details about the proposed analytical nonlinear spring model are given in Supporting Information Note S8.

Acknowledgments

X.S.Z. and W.L. acknowledge the support from U.S. National Science Foundation (NSF) CAREER Award CMMI-2047692. O.S. and F.W. acknowledge the support from the Villum Foundation Villum Investigator Project “InnoTop". We thank the service provided by Advanced Materials Testing and Evaluation Laboratory (AMTEL) of University of Illinois Urbana-Champaign.

1. B Mosadegh, et al., Pneumatic networks for soft robotics that actuate rapidly. *Adv. Funct. Mater.* **24**, 2163–2170 (2014).
2. B Gorissen, D Melancon, N Vasios, M Torbati, K Bertoldi, Inflatable soft jumper inspired by shell snapping. *Sci. Robotics* **5** (2020).
3. K Liu, F Hacker, C Daraio, Robotic surfaces with reversible, spatiotemporal control for shape morphing and object manipulation. *Sci. Robotics* **6** (2021).
4. T Frenzel, C Findeisen, M Kadic, P Gumbsch, M Wegener, Tailored buckling microlattices as reusable light-weight shock absorbers. *Adv. Mater.* **28**, 5865–5870 (2016).
5. K Fu, Z Zhao, L Jin, Programmable granular metamaterials for reusable energy absorption. *Adv. Funct. Mater.* **29**, 1901258 (2019).
6. S Yuan, CK Chua, K Zhou, 3d-printed mechanical metamaterials with high energy absorption. *Adv. Mater. Technol.* **4**, 1800419 (2019).
7. F Pan, et al., 3d pixel mechanical metamaterials. *Adv. Mater.* **31**, 1900548 (2019).
8. S Shan, et al., Multistable architected materials for trapping elastic strain energy. *Adv. Mater.* **27**, 4296–4301 (2015).
9. DH Kim, et al., Epidermal electronics. *Science* **333**, 838–843 (2011).
10. KI Jang, et al., Soft network composite materials with deterministic and bio-inspired designs. *Nat. Commun.* **6**, 6566 (2015).
11. H Chen, et al., The equivalent medium of cellular substrate under large stretching, with applications to stretchable electronics. *J. Mech. Phys. Solids* **120**, 199–207 (2018) Special issue in honor of Ares J. Rosakis on the occasion of his 60th birthday.
12. Z Xue, H Song, JA Rogers, Y Zhang, Y Huang, Mechanically-guided structural designs in stretchable inorganic electronics. *Adv. Mater.* **32**, 1902254 (2020).
13. K Bertoldi, PM Reis, S Willshaw, T Mullin, Negative poisson’s ratio behavior induced by an elastic instability. *Adv. Mater.* **22**, 361–366 (2010).
14. J Shim, et al., Harnessing instabilities for design of soft reconfigurable auxetic/chiral materials. *Soft Matter* **9**, 8198–8202 (2013).
15. F Wang, O Sigmund, J Jensen, Design of materials with prescribed nonlinear properties. *J. Mech. Phys. Solids* **69**, 156 – 174 (2014).
16. A Clausen, F Wang, JS Jensen, O Sigmund, JA Lewis, Topology optimized architectures with programmable poisson’s ratio over large deformations. *Adv. Mater.* **27**, 5523–5527 (2015).
17. A Rafsanjani, A Akbarzadeh, D Pasini, Snapping mechanical metamaterials under tension. *Adv. Mater.* **27**, 5931–5935 (2015).
18. K Che, C Yuan, J Wu, H Jerry Qi, J Meaud, Three-dimensional-printed multistable mechanical metamaterials with a deterministic deformation sequence. *J. Appl. Mech.* **84** (2016) 011004.
19. OR Bilal, R Süsstrunk, C Daraio, SD Huber, Intrinsically polar elastic metamaterials. *Adv. Mater.* **29**, 1700540 (2017).
20. H Yuk, X Zhao, A new 3d printing strategy by harnessing deformation, instability, and fracture of viscoelastic inks. *Adv. Mater.* **30**, 1704028 (2018).
21. E Medina, PE Farrell, K Bertoldi, CH Rycroft, Navigating the landscape of nonlinear mechanical metamaterials for advanced programmability. *Phys. Rev. B* **101**, 064101 (2020).
22. X Kuang, et al., Magnetic dynamic polymers for modular assembling and reconfigurable morphing architectures. *Adv. Mater.* **33**, 2102113 (2021).
23. Y Li, Q Zhang, Y Hong, J Yin, 3d transformable modular kirigami based programmable metamaterials. *Adv. Funct. Mater.* **31**, 2105641 (2021).
24. X Lin, et al., A stair-building strategy for tailoring mechanical behavior of re-customizable metamaterials. *Adv. Funct. Mater.* **31**, 2101808 (2021).
25. Q Zhang, D Guo, G Hu, Tailored mechanical metamaterials with programmable quasi-zero-stiffness features for full-band vibration isolation. *Adv. Funct. Mater.* **31**, 2101428 (2021).
26. B Florijn, C Coulais, M van Hecke, Programmable mechanical metamaterials. *Phys. Rev. Lett.* **113**, 175503 (2014).
27. W Li, F Wang, O Sigmund, XS Zhang, Design of composite structures with programmable elastic responses under finite deformations. *J. Mech. Phys. Solids* **151**, 104356 (2021).
28. D Høj, et al., Ultra-coherent nanomechanical resonators based on inverse design. *Nat. Commun.* **12**, 5766 (2021).
29. Z Jia, et al., Microstructural design for mechanical–optical multifunctionality in the exoskeleton of the flower beetle torynorrhina flammea. *Proc. Natl. Acad. Sci.* **118** (2021).
30. MP Bendsøe, O Sigmund, *Topology Optimization: Theory, Methods and Applications*. (Springer, Berlin, Heidelberg), (2003).
31. JW Boley, et al., Shape-shifting structured lattices via multimaterial 4d printing. *Proc. Natl. Acad. Sci.* **116**, 20856–20862 (2019).
32. H Fang, SCA Chu, Y Xia, KW Wang, Programmable self-locking origami mechanical metamaterials. *Adv. Mater.* **30**, 1706311 (2018).

33. ME Pontecorvo, S Barbarino, GJ Murray, FS Gandhi, Bistable arches for morphing applications. *J. Intell. Material Syst. Struct.* **24**, 274–286 (2013).
34. IK Kuder, AF Arrieta, WE Raither, P Ermanni, Variable stiffness material and structural concepts for morphing applications. *Prog. Aerosp. Sci.* **63**, 33–55 (2013).
35. A Zareei, B Deng, K Bertoldi, Harnessing transition waves to realize deployable structures. *Proc. Natl. Acad. Sci.* **117**, 4015–4020 (2020).
36. N Friedman, A Ibrahimbegovic, Overview of highly flexible, deployable lattice structures used in architecture and civil engineering undergoing large displacements. *YBL J. Built Environ.* **1**, 85–103 (2013).